Stanford Exploration Project, Report 117, October 23, 2004, pages 63–77

Target-oriented computation of the wave-equation imaging Hessian

Alejandro A. Valenciano and Biondo Biondi[1]

ABSTRACT

A target-oriented strategy can be applied to explicitly compute the wave-equation imaging Hessian. This approach allows us to study the characteristics of the Hessian for different acquisition and subsurface geometries (low illumination, faults, etc.). Results on the Sigsbee and the Marmousi model show that in complex areas, a diagonal approximation of the Hessian might be insufficient to obtain the correct position and amplitudes of the reflectors.

INTRODUCTION

Seismic imaging (migration) operators are non-unitary (Claerbout, 1992) because they depend on: (1) the seismic experiment acquisition geometry (Nemeth et al., 1999; Duquet and Marfurt, 1999; Ronen and Liner, 2000), (2) the complex subsurface geometry (Prucha et al., 2000; Kuehl and Sacchi, 2001) and (3), the bandlimited characteristics of the seismic data (Chavent and Plessix, 1999). Often, they produce images with reflectors correctly positioned but with biased amplitudes.

Attempts to solve this problem have used the power of geophysical inverse theory (Tarantola, 1987), which compensates for the experimental deficiencies (acquisition geometry, obstacles, etc.) by weighting the migration result with the inverse of the Hessian. The main difficulty with this approach is the explicit calculation of the inverse of the Hessian. However, in most of the situations, the direct computation of its inverse for the entire model space is practically unfeasible.

Three different paths have been followed to practically approximate the inverse of the Hessian. The first approach approximates the Hessian as a diagonal matrix (Chavent and Plessix, 1999; Rickett, 2003), which makes its inversion trivial. The second approach makes use of iterative algorithms like conjugate-gradient (Nemeth et al., 1999; Duquet and Marfurt, 1999; Ronen and Liner, 2000; Prucha et al., 2000; Kuehl and Sacchi, 2001) to implicitly calculate the inverse of the Hessian. The third approach (Guitton, 2004) approximates the inverse of the Hessian with a bank of nonstationary matching filters.

Since accurate imaging of reflectors is more important at the reservoir level, we propose

[1]**email:** valencia@sep.stanford.edu, biondo@sep.stanford.edu

calculating the Hessian in a target-oriented fashion. This can be done in practice, since the new dimensions of the Hessian (in the target region alone) are smaller than the dimensions of the whole image. By knowing the characteristics of the exact Hessian, an educated choice can be made regarding how to approximate its inverse.

In this paper, we first discuss how the target-oriented Hessian can be calculated from precomputed Green functions. We also show three numerical examples of target-oriented computed Hessians, the first in a constant velocity model, the second in the Sigsbee model (to study the effects of poor illumination in the Hessian), and the third in the Marmousi model.

LINEAR LEAST-SQUARES INVERSION

Tarantola (1987) formalizes the geophysical inverse problem by giving a theoretical approach to compensate for the experiment's deficiencies (acquisition geometry, obstacles, etc.), while being consistent with the acquired data. His approach can be summarized as follows: given a linear modeling operator $\mathbf{L}$ to compute synthetic data $\mathbf{d}$,

$$\mathbf{d} = \mathbf{L}\mathbf{m}, \tag{1}$$

where $\mathbf{m}$ is a reflectivity model, and given the recorded data $\mathbf{d}_{obs}$, a quadratic cost function

$$S(\mathbf{m}) = \|\mathbf{d} - \mathbf{d}_{obs}\|^2 = \|\mathbf{L}\mathbf{m} - \mathbf{d}_{obs}\|^2 \tag{2}$$

is formed. The model of the earth $\hat{\mathbf{m}}$ that minimize $S(\mathbf{m})$ is given by

$$\hat{\mathbf{m}} = (\mathbf{L}'\mathbf{L})^{-1}\mathbf{L}'\mathbf{d}_{obs} = \mathbf{H}^{-1}\mathbf{L}'\mathbf{d}_{obs}, \tag{3}$$

where $\mathbf{L}'$ is the adjoint of the linear operator $\mathbf{L}$, and $\mathbf{H} = \mathbf{L}'\mathbf{L}$ is the Hessian of $S(\mathbf{m})$.

The main difficulty with this approach is that the explicit calculation of inverse of the Hessian for the entire model space is practically unfeasible. That is why iterative algorithms like conjugate-gradient have been used to implicitly calculate the inverse of the Hessian (Nemeth et al., 1999; Duquet and Marfurt, 1999; Ronen and Liner, 2000; Prucha et al., 2000; Kuehl and Sacchi, 2001).

In the case of wave-equation migration or inversion, the operator $\mathbf{L}$ is expensive to apply. Thus, applying this operator and its transpose iteratively is sometimes prohibitive. Among other factors, the computational cost is proportional to the number of depth steps the wavefields need to be propagated (Audebert, 1994), and the number of iterations.

TARGET-ORIENTED HESSIAN

Since accurate imaging of reflectors is more important in the neighborhood of the reservoir, it makes sense to apply a target-oriented strategy to reduce the number of depth steps. A way to achieve this objective is to write the modeling operator $\mathbf{L}$ in a target-oriented fashion and explicitly compute the Hessian.

In general, the synthetic data for one frequency, a shot positioned at $\mathbf{x}_s = (0, x_s, y_s)$ and a receiver positioned at $\mathbf{x}_r = (0, x_r, y_r)$ can be given by a linear operator $\mathbf{L}$ acting on the full model space $\mathbf{m}(\mathbf{x})$ with $\mathbf{x} = (z, x, y)$ ($\mathbf{x} = (z, x)$ in $2D$) as

$$\mathbf{d}(\mathbf{x}_s, \mathbf{x}_r; \omega) = \mathbf{L}\mathbf{m}(\mathbf{x}) = \sum_{\mathbf{x}} \mathbf{G}(\mathbf{x}, \mathbf{x}_s; \omega)\, \mathbf{G}(\mathbf{x}, \mathbf{x}_r; \omega)\, \mathbf{m}(\mathbf{x}), \tag{4}$$

where $\mathbf{G}(\mathbf{x}, \mathbf{x}_s; \omega)$ and $\mathbf{G}(\mathbf{x}, \mathbf{x}_r; \omega)$ are the Green functions from the shot position $\mathbf{x}_s$ and the receiver position $\mathbf{x}_r$ to a point in the model space $\mathbf{x}$.

In equation (4), two important properties have been used (Ehinger et al., 1996): first, the Green functions are computed by means of the one-way wave equation, and second, the extrapolation is performed by using the adequate paraxial wave equations (flux conservation) (Bamberger et al., 1988).

The quadratic cost function is

$$S(\mathbf{m}) = \sum_{\omega} \sum_{\mathbf{x}_s} \sum_{\mathbf{x}_r} \|\mathbf{d} - \mathbf{d}_{obs}\|^2 = \sum_{\omega} \sum_{\mathbf{x}_s} \sum_{\mathbf{x}_r} [\mathbf{d}(\mathbf{x}_s, \mathbf{x}_r; \omega) - \mathbf{d}_{obs}]' [\mathbf{d}(\mathbf{x}_s, \mathbf{x}_r; \omega) - \mathbf{d}_{obs}], \tag{5}$$

and its second derivative with respect to the model parameters $\mathbf{m}(\mathbf{x})$ and $\mathbf{m}(\mathbf{y})$ is the Hessian

$$\mathbf{H}(\mathbf{x}, \mathbf{y}) = \frac{\partial^2 S(\mathbf{m})}{\partial \mathbf{m}(\mathbf{x}) \partial \mathbf{m}(\mathbf{y})} = \sum_{\omega} \sum_{\mathbf{x}_s} \sum_{\mathbf{x}_r} \left[\frac{\partial \mathbf{d}(\mathbf{x}_s, \mathbf{x}_r; \omega)}{\partial \mathbf{m}(\mathbf{x})} \right]' \left[\frac{\partial \mathbf{d}(\mathbf{x}_s, \mathbf{x}_r; \omega)}{\partial \mathbf{m}(\mathbf{y})} \right] \tag{6}$$

$$\mathbf{H}(\mathbf{x}, \mathbf{y}) = \sum_{\omega} \sum_{\mathbf{x}_s} \mathbf{G}'(\mathbf{x}, \mathbf{x}_s; \omega) \mathbf{G}(\mathbf{y}, \mathbf{x}_s; \omega) \sum_{\mathbf{x}_r} \mathbf{G}'(\mathbf{x}, \mathbf{x}_r; \omega) \mathbf{G}(\mathbf{y}, \mathbf{x}_r; \omega). \tag{7}$$

Notice that to compute $\mathbf{H}(\mathbf{x}, \mathbf{y})$ in equation (7), only the precomputed Green functions at model points $\mathbf{x}$ and $\mathbf{y}$ are needed. Thus, the size of the problem can be considerably reduced by storing the Green functions only at the target location $\mathbf{x}_T$. Then equation (7) reduces to

$$\mathbf{H}(\mathbf{x}_T, \mathbf{y}_T) = \sum_{\omega} \sum_{\mathbf{x}_s} \mathbf{G}'(\mathbf{x}_T, \mathbf{x}_s; \omega) \mathbf{G}(\mathbf{y}_T, \mathbf{x}_s; \omega) \sum_{\mathbf{x}_r} \mathbf{G}'(\mathbf{x}_T, \mathbf{x}_r; \omega) \mathbf{G}(\mathbf{y}_T, \mathbf{x}_r; \omega), \tag{8}$$

where the Hessian is computed only at the target location.

In the next section we show three numerical examples of Hessians estimated with the proposed target-oriented approach.

NUMERICAL EXAMPLES

In this section we show three numerical examples of target-oriented computed Hessians. The first Hessian is estimated in a constant velocity model, the second in the Sigsbee model (to study the effects of poor illumination in the Hessian), and the third in the Marmousi model (to study the effect of faults in the Hessian).

Constant-velocity model

It is possible to explicitly compute the Hessian for small models, or if a target-oriented strategy is followed. We created a synthetic data set assuming a land-type acquisition geometry: the shots were positioned every 25 m from $x = -0.8\ km$ to $x = 0.8\ km$, keeping fixed receivers from $x = -0.8\ km$ to $x = 0.8\ km$. Figures 1a and 1b show the Hessian matrix of the constant-velocity model. Notice the banded nature of the matrix (Figure 1b), with most of the energy in the main diagonal (Chavent and Plessix, 1999). At the extremes of the diagonal the amplitudes become dimmer (Figure 1a) indicating points of lower illumination at the extremes of the acquisition.

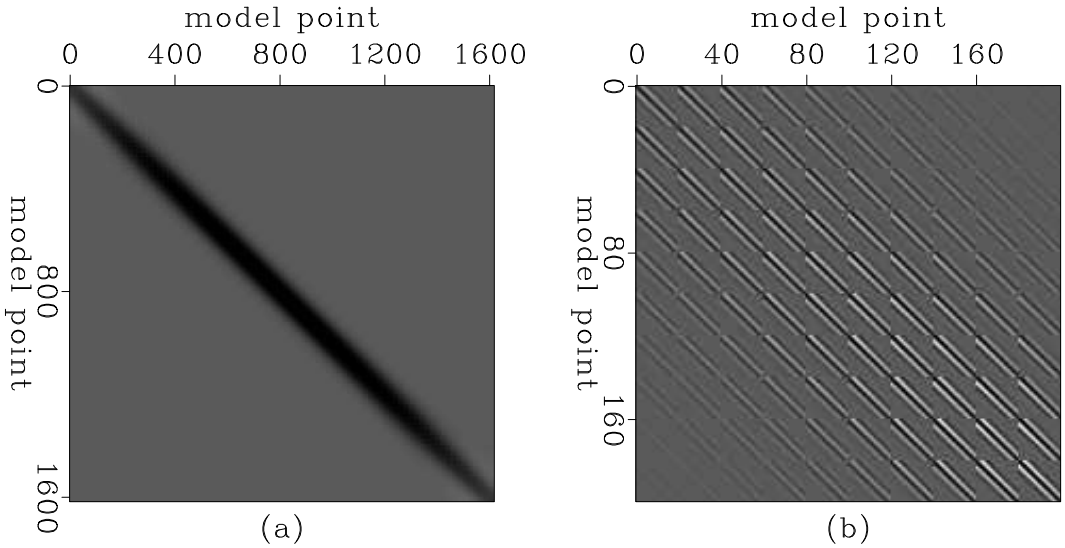

Figure 1: (a) Hessian matrix of the constant-velocity model, and, (b) close-up of Figure 1a. alejandro1-hmatrix_const [CR]

For a fixed point $\mathbf{x}$, each line of the Hessian $\mathbf{H}(\mathbf{x},\mathbf{y})$ can be mapped to a grid the size of the model space. Figures 2 and 3 show the Hessian and the envelope of the Hessian at four different fixed points. The Hessian (Figure 2) has phase information that can make it difficult to interpret in complex subsurface geometries (see Sigsbee and Marmousi model case), therefore we based our analysis looking at the envelope of the Hessian, (Figure 3), which shows clearly the main features of interest.

Figure 3a shows point 1, with coordinates $\mathbf{x} = (0.2, 0)$ (at the center of the acquisition). Notice the size of the ellipse and the orientation of the principal semi-axis perpendicular to the x axis. Figure 3b shows point 2, with coordinates $\mathbf{x} = (0.8, 0)$. Notice that the ellipse is bigger than the ellipse corresponding to point 1 (the size of the ellipse depends on the deph and background velocity (Chavent and Plessix, 1999)), and also that the orientation of the principal semi-axis is perpendicular to the x axis. Figures 3c and 3d show points 3 and 4, with coordinates $\mathbf{x} = (0.2, -0.6)$ and $\mathbf{x} = (0.2, 0.6)$, respectively (opposite sides of the center of the acquisition). Notice the size of the ellipses are the same, but the orientation of the principal semi-axes are tilted in opposite directions. The energy of the ellipses become dimmer than the

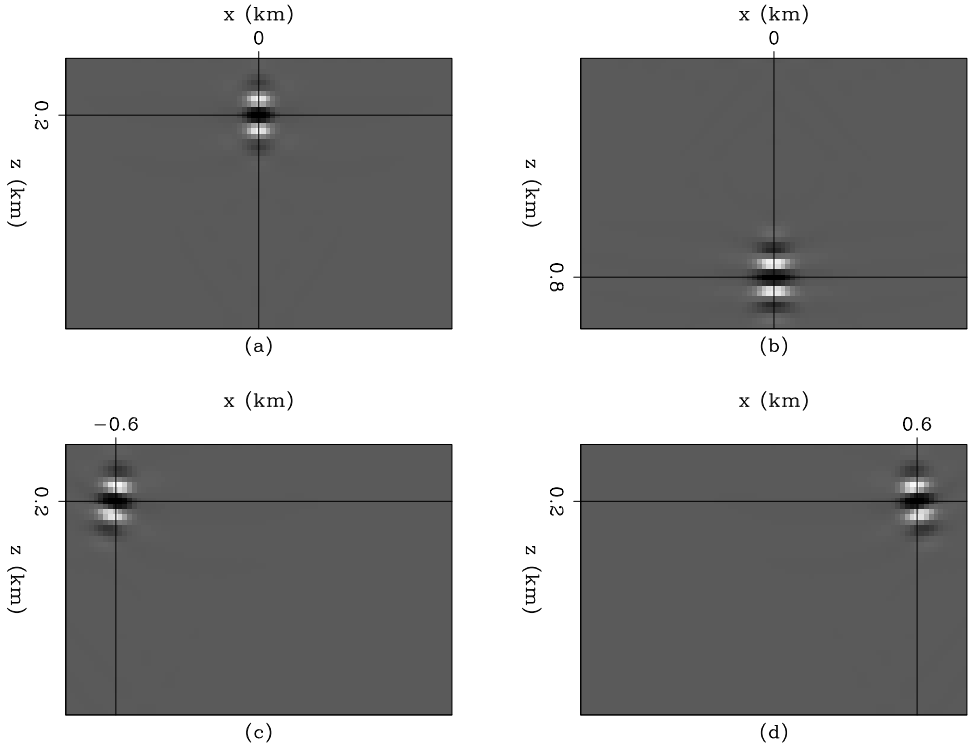

Figure 2: Hessian of the constant-velocity model, (a) point 1, (b) point 2, (c) point 3, and (d) point 4. alejandro1-hesian_phase_const [CR]

one in the center, indicating that these points have lower illumination.

Sigsbee model

The Sigsbee data set was modeled by simulating the geological setting found on the Sigsbee escarpment in the deep-water Gulf of Mexico. The model exhibits the illumination problems due to the complex salt shape, with a rugose salt top (Figure 4) found in this area. We choose a target zone (indicated with the "target" box in Figure 4) to see the effects of illumination on the Hessian close to the salt.

Figures 5a and 5b show the Hessian matrix for the Sigsbee model. Notice the banded nature of the matrix (Figure 5b), with most of the energy on the main diagonal (Figure 5a). As opposed to the case with the constant-velocity, the energy decreases considerably in some areas of the diagonal due to illumination problems cause by the salt body. But, similar to the constant velocity case, amplitudes become dimmer at the extremes of the diagonal due to the acquisition geometry.

We fixed seven points, all of them at the same depth, to see the corresponding lines of the Hessian. Figures 6 and 7 show the Hessian and the envelope of the Hessian, respectively. The envelope of the Hessian (Figure 7) shows clearly the main features of interest.

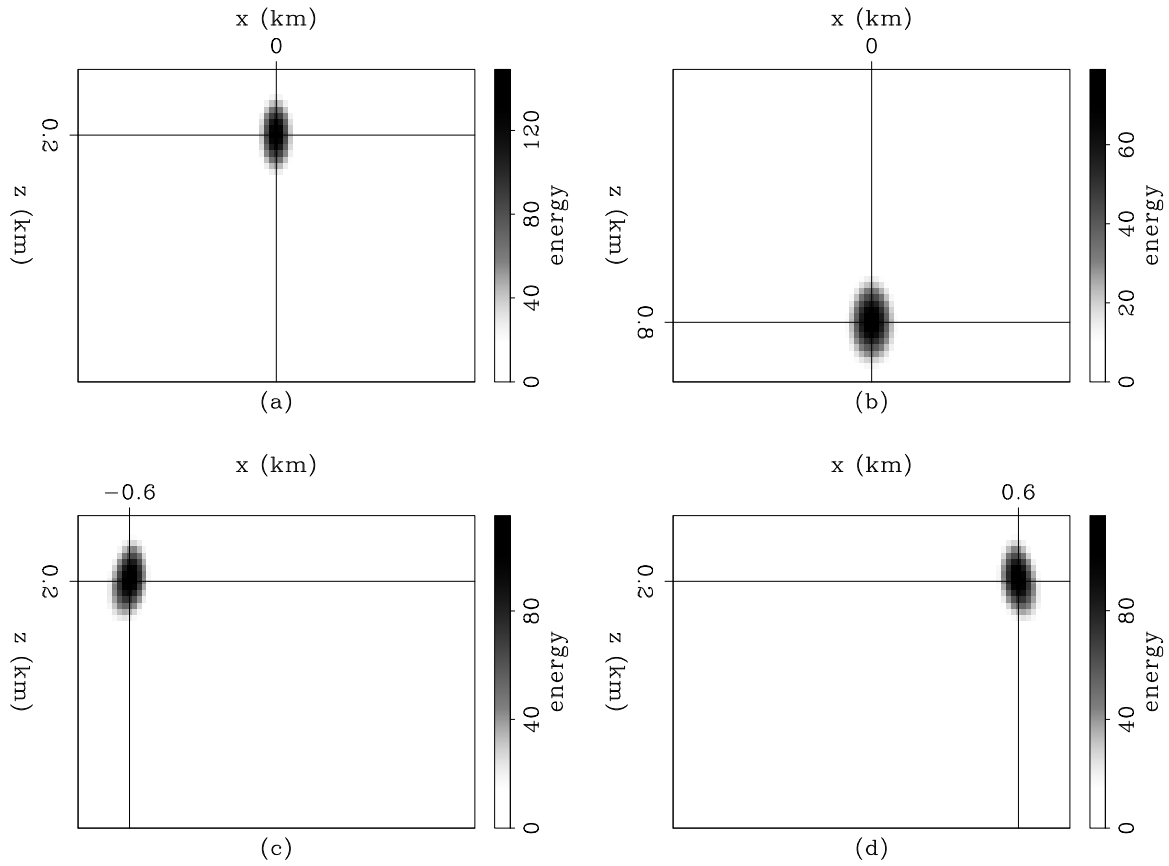

Figure 3: Envelope of the Hessian of the constant-velocity model, (a) point 1, (b) point 2, (c) point 3, and (d) point 4. alejandro1-hesian_const [CR]

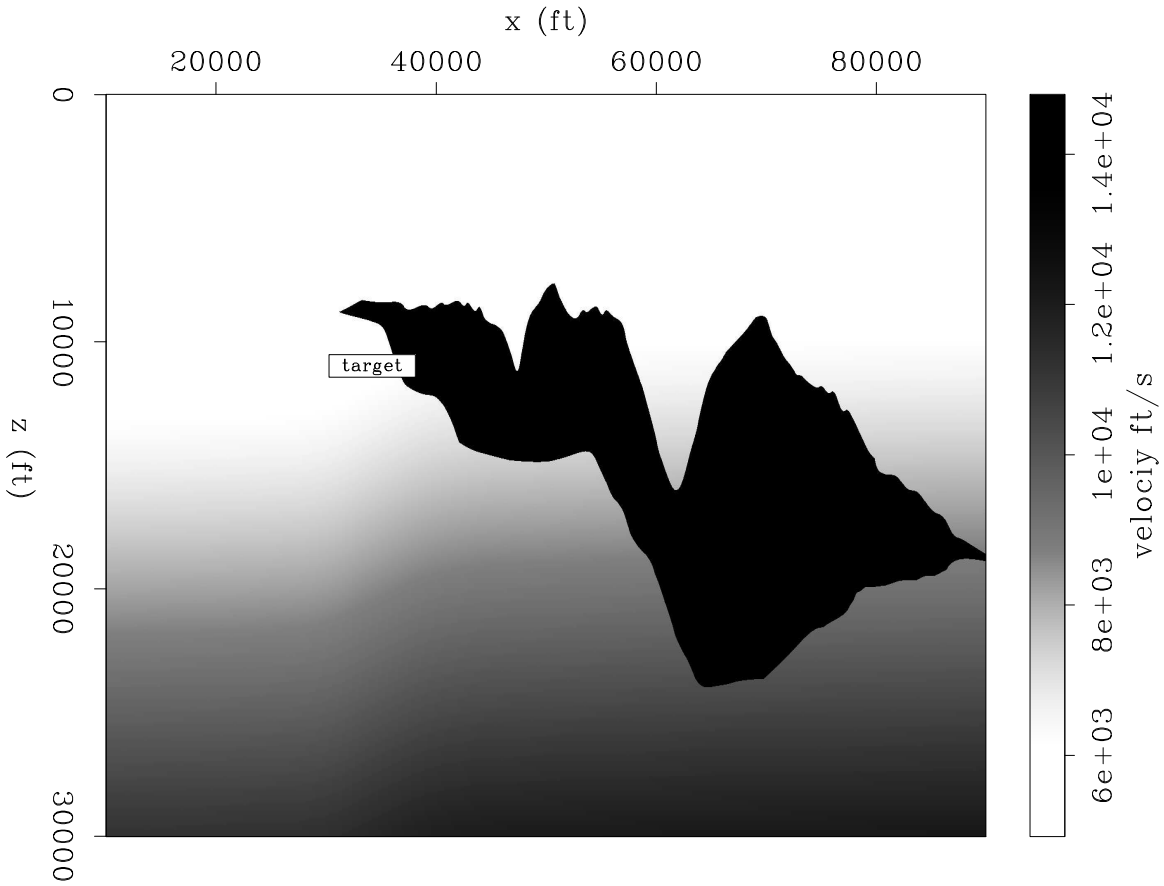

Figure 4: Sigsbee velocity model, target zone indicated with the "target" box. alejandro1-Sis_vel [ER]

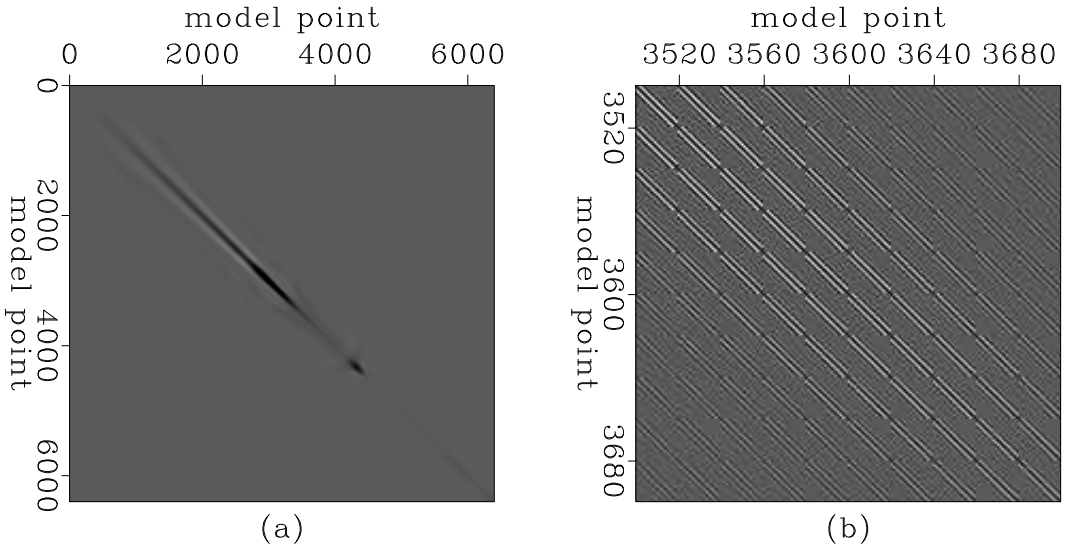

Figure 5: Hessian matrix of the Sigsbee velocity model. alejandro1-hmatrix_Sis [CR]

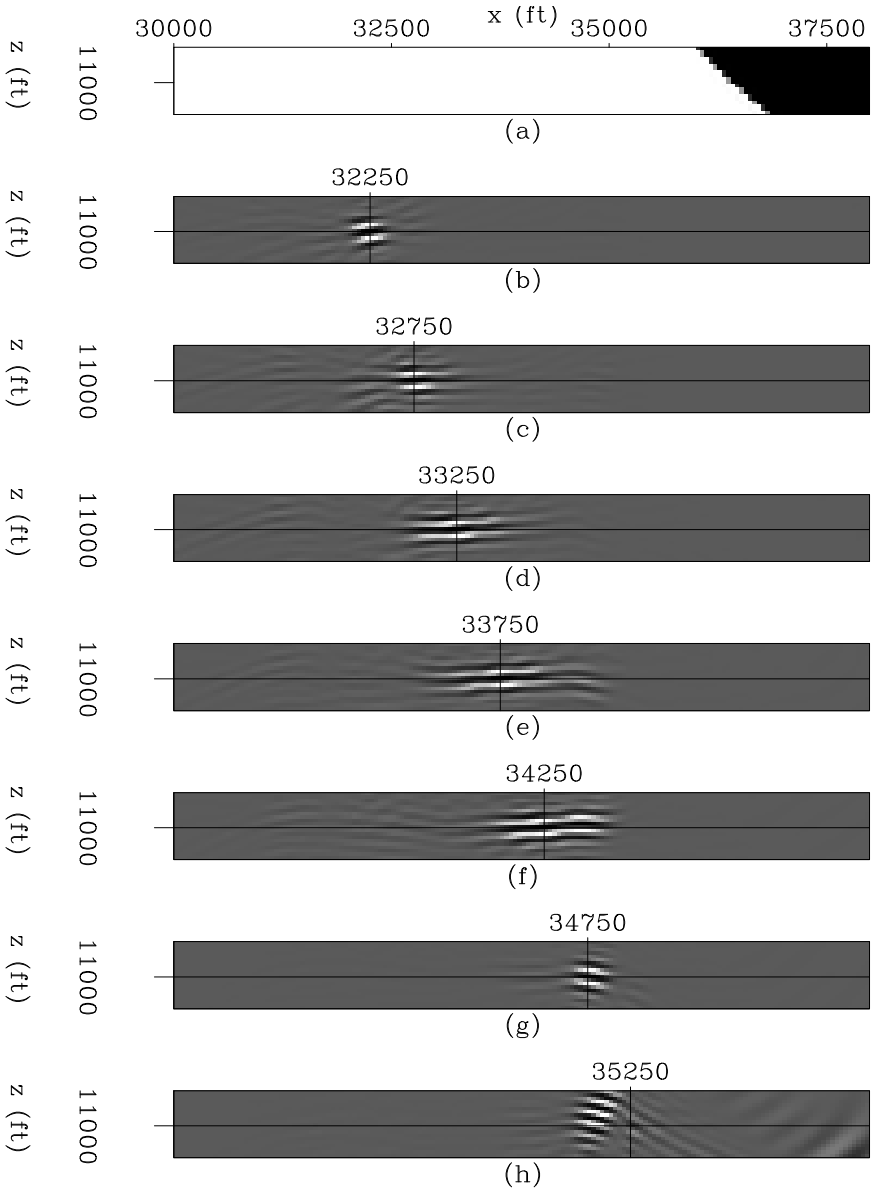

Figure 6: Hessian of the constant-velocity model, (a) Close-up of the Sigsbee velocity model (salt body to the right and sediments to the left), (b) point 1, (c) point 2, (d) point 3, (e) point 4, (f) point 5, (g) point 6, and (h) point 7. alejandro1-hesian_phase_Sis [CR]

Figure 7a shows a close-up of the velocity model in the area where the target-oriented Hessian was computed (salt body to the right and sediments to the left). Figure 7b shows point 1, with coordinates $\mathbf{x} = (11000, 32250)$; since this point in the model is well illuminated, the resulting ellipse looks similar to the constant-velocity ellipses. Figures 7c-7f show points 2 to 5, with coordinates $\mathbf{x} = (11000, 32750)$, $\mathbf{x} = (11000, 33250)$, $\mathbf{x} = (11000, 33750)$, and $\mathbf{x} = (11000, 34250)$, respectively. As the points enter a shadow zone, the ellipses lose energy and splits. A diagonal matrix approximation of the Hessian would not be appropriate to describe this behavior, since there is considerable energy away from the point where the ellipse should be centered. Figure 7g shows point 6, with coordinates $\mathbf{x} = (11000, 347500)$; out of the shadow zone, the ellipse gains energy.

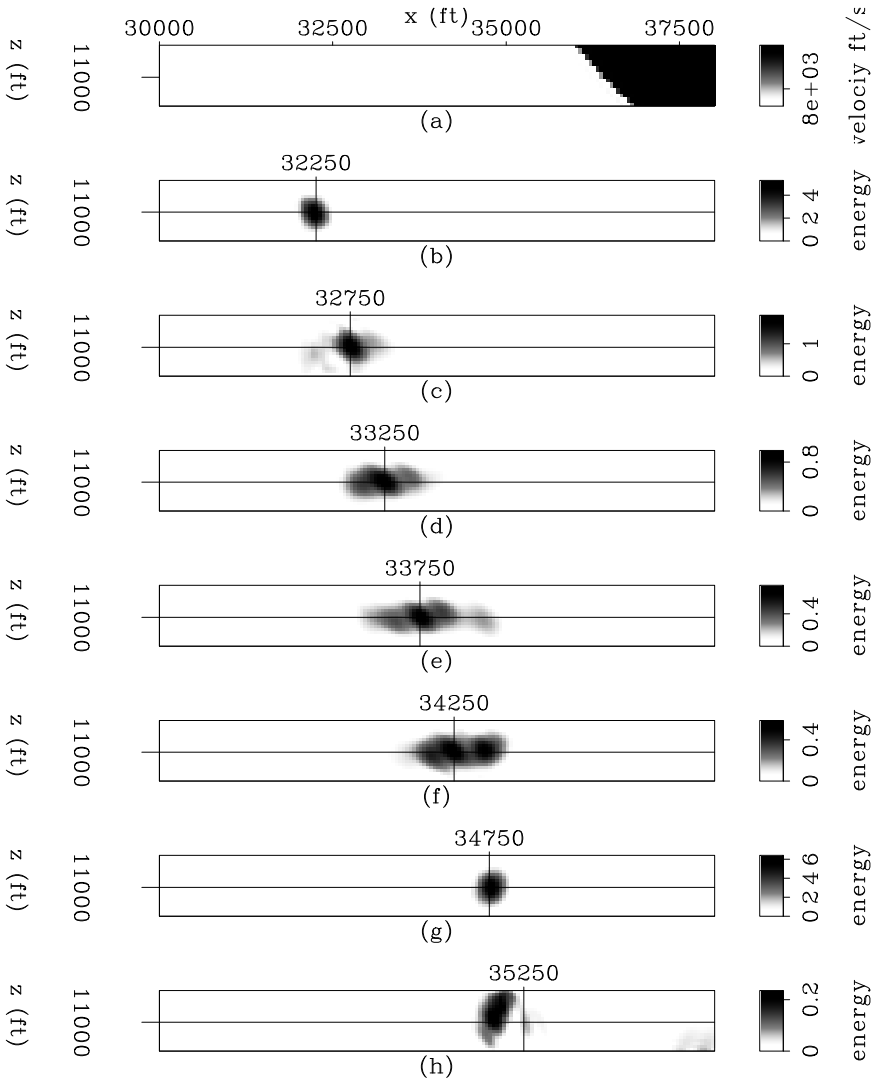

Figure 7: Envelope of the Hessian of the constant-velocity model, (a) Close-up of the Sigsbee velocity model (salt body to the right and sediments to the left), (b) point 1, (c) point 2, (d) point 3, (e) point 4, (f) point 5, (g) point 6, and (h) point 7. alejandro1-hesian_Sis [CR]

Finally, Figure 7h shows point 7, with coordinates $\mathbf{x} = (11000, 35250)$. As the point gets

closer to the salt boundary it enters a new shadow zone. This point behaves differently, the Hessian not only losses energy but the ellipse center is away from where it should be. This behavior might suggest that not enough reference velocities where used in the split-step computation of the Green functions. Or more fundamentally, that the physics of wave propagation is not well modeled by the acoustic one-way wave-equation close to the salt. This subject deserves more attention in the future.

Marmousi model

The Marmousi synthetic data set (Bourgeois et al., 1991) was first released as a blind test for velocity estimation. It has become a popular testbed for migration algorithms. Its structural style is dominated by growth faults, which arise from salt creep and give rise to the complicated velocity structure in the upper part of the model (Figure 8). We choose a target zone (indicated with the "target" box in Figure 8) to see the effects of the faults on the Hessian.

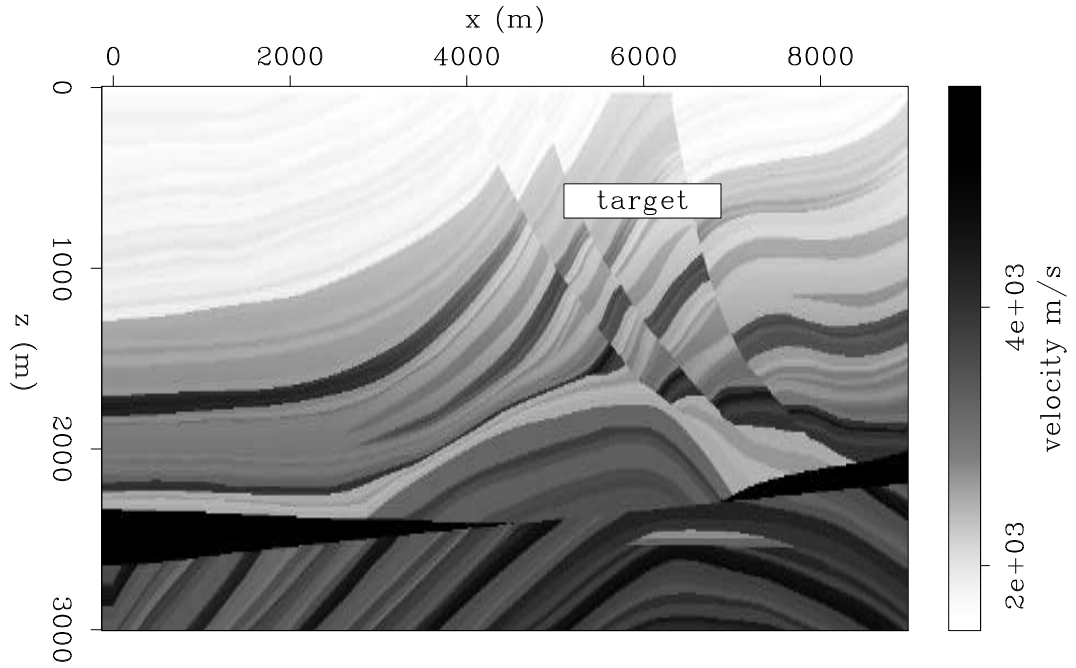

Figure 8: Marmousi velocity model. alejandro1-Marm_vel [ER]

Figures 9a and 9b show the Hessian matrix of the Marmousi model. Notice the banded nature of the matrix (Figure 9b), with most of the energy in the main diagonal (Figure 9a). There are changes of the energy in the diagonal, but not as strong as for the Sigsbee model case.

We fixed four points to see the lines of the Hessian corresponding to different geological features in the model. Figures 10 and 11 show the Hessian and the envelope of the Hessian, respectively. The envelope of the Hessian (Figure 11) shows clearly the main features of interest.

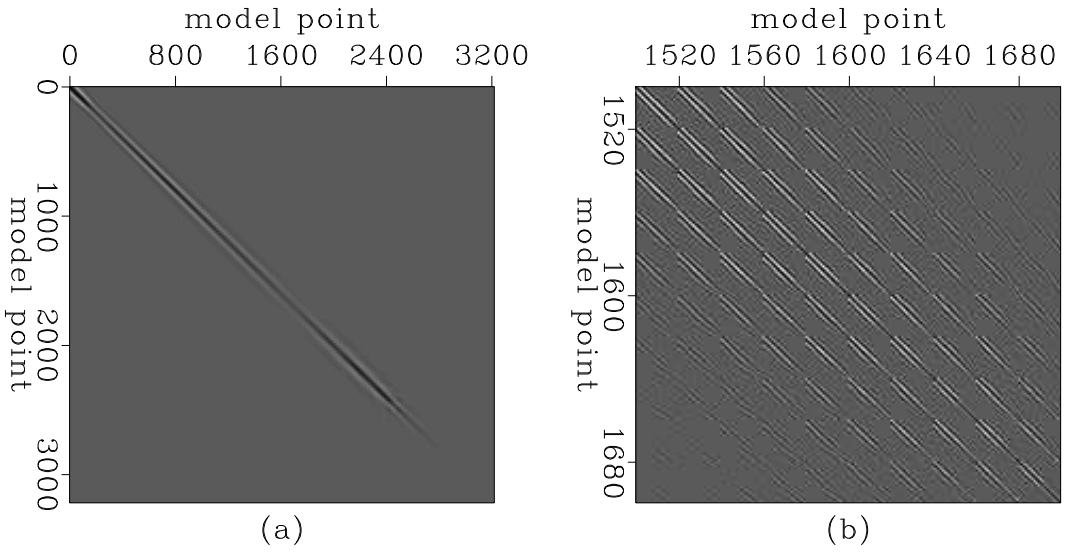

Figure 9: Hessian matrix of the Marmousi model. alejandro1-hmatrix_marm [CR]

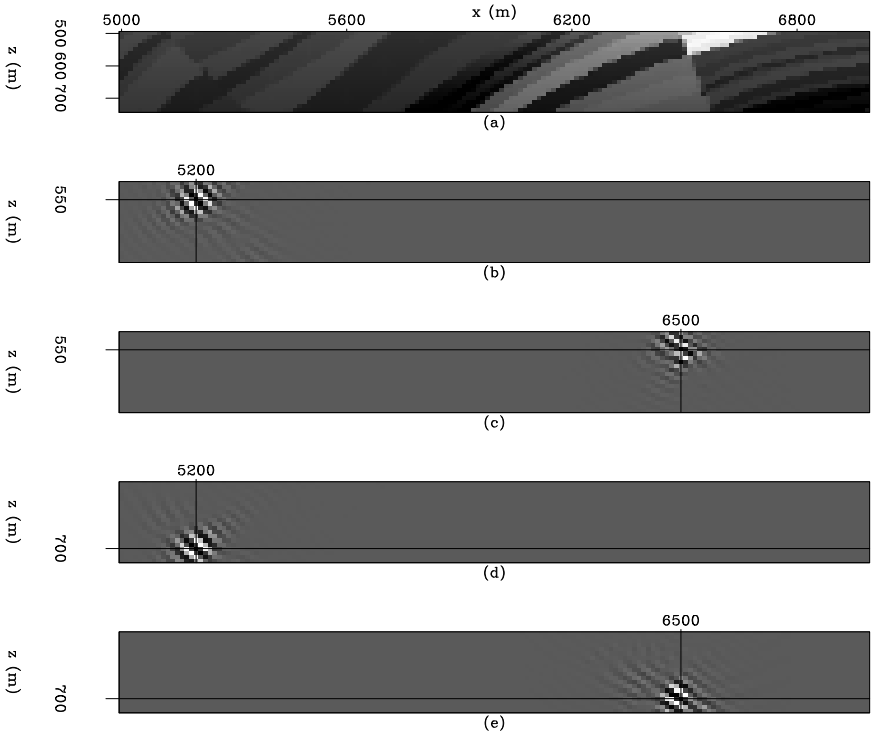

Figure 10: Hessian of the Marmousi model,(a) Close-up of the Marmousi velocity model, (b) point 1, (c) point 2, (d) point 3, and (e) point 4. alejandro1-hesian_phase_marm [CR]

Figure 11a shows a close-up of the velocity model in the area where the target-oriented Hessian was computed. Figure 11b shows point 1, with coordinates $\mathbf{x} = (550, 5200)$. Since this point in the model is well illuminated, the resulting ellipse looks similar to the constant-velocity ellipses. Figure 7c shows point 2, with coordinates $\mathbf{x} = (550, 6500)$. Notice that this point is close to a fault, producing a distortion to the ellipse shape. Figure 11d shows point 3, with coordinates $\mathbf{x} = (700, 5200)$; as with point 1, the ellipse is not distorted. Finally, Figure 7e shows point 4, with coordinates $\mathbf{x} = (700, 6500)$. This point is also close to the fault, but the velocity contrast across the fault is smaller, producing less distortion than in the point 3 case.

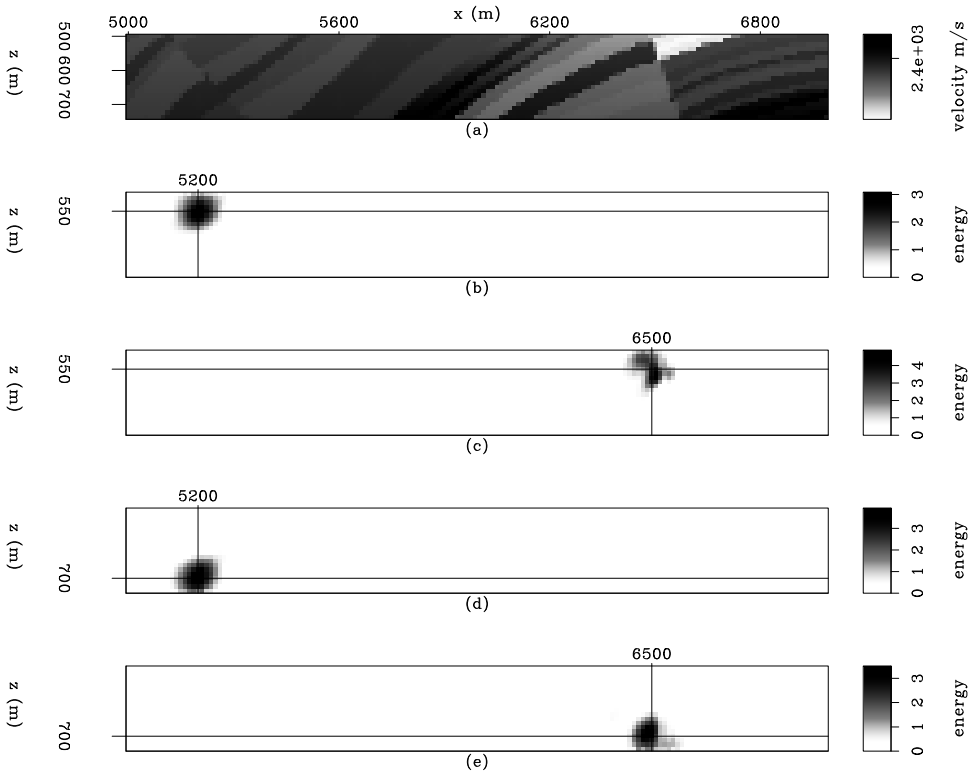

Figure 11: Envelope of the Hessian of the Marmousi model,(a) Close-up of the Marmousi velocity model, (b) point 1, (c) point 2, (d) point 3, and (e) point 4. alejandro1-hesian_marm [CR]

CONCLUSIONS

Since accurate imaging of reflections is more important in the neighborhood of the reservoir, a target-oriented strategy can be applied to explicitly compute the inversion Hessian. This allows us to study the characteristics of the Hessian in different acquisition geometries and subsurface situations (low illumination, faults, etc.) and will make possible the design of a strategy to approximate its inverse.

Results on the Sigsbee model show that inside the shadow zones, the Hessian ellipses split

and reduce their energy. Something different happened close to faults, as can be seen in the Marmousi model. There, the Hessian ellipses are distorted but do not split. The latest results suggest that in complex areas the usual diagonal-matrix approximation of the Hessian might be insufficient to obtain the correct position and amplitude of the reflectors.

ACKNOWLEDGMENTS

We would like to thank SMAART JV for the Sigsbee dataset used in our experiments.

REFERENCES

Audebert, F., 1994, 3-D prestack depth migration: Why Kirchhoff?: SEP–**80**, 191–208.

Bamberger, A., Engquist, B., Halpern, L., and Joly, P., 1988, Paraxial approximation in heterogeneous media: SIAM J. Appl. Math., **48**, 98–128.

Bourgeois, A., Bourget, M., Lailly, P., Poulet, M., Ricarte, P., and Versteeg, R., 1991, Marmousi, model and data: Proceedings of 1990 EAEG workshop on practical aspects of seismic data inversion.

Chavent, G., and Plessix, R. E., 1999, An optimal true-amplitude least-squares prestack depth-migration operator: Geophysics, **64**, no. 2, 508–515.

Claerbout, J. F., 1992, Earth soundings analysis, processing versus inversion: Blackwell Scientific Publications.

Duquet, B., and Marfurt, K. J., 1999, Filtering coherent noise during prestack depth migration: Geophysics, **64**, no. 4, 1054–1066.

Ehinger, A., Lailly, P., and Marfurt, K. J., 1996, Green's function implementation of common-offset wave-equation migration: Geophysics, **61**, no. 06, 1813–1821.

Guitton, A., 2004, Amplitude and kinematic corrections of migrated images for nonunitary imaging operators: Geophysics, **69**, no. 04, 1017–1024.

Kuehl, H., and Sacchi, M., 2001, Generalized least-squares DSR migration using a common angle imaging condtion: Soc. of Expl. Geophys., 71st Ann. Internat. Mtg, 1025–1028.

Nemeth, T., Wu, C., and Schuster, G. T., 1999, Least-squares migration of incomplete reflection data: Geophysics, **64**, no. 1, 208–221.

Prucha, M. L., Clapp, R. G., and Biondi, B., 2000, Seismic image regularization in the reflection angle domain: SEP–**103**, 109–119.

Rickett, J. E., 2003, Illumination-based normalization for wave-equation depth migration: Geophysics, **68**, no. 04, 1371–1379.

Ronen, S., and Liner, C. L., 2000, Least-squares DMO and migration: Geophysics, **65**, no. 5, 1364–1371.

Tarantola, A., 1987, Inverse problem theory: Elsevier.